



## Cu/Ag EAM potential optimized for heteroepitaxial diffusion from *ab initio* data

Henry H. Wu\*, Dallas R. Trinkle

Department of Materials Science and Engineering, University of Illinois, Urbana-Champaign 61801, United States

### ARTICLE INFO

#### Article history:

Received 24 August 2009

Accepted 29 September 2009

Available online 6 November 2009

#### Keywords:

Surface diffusion

Heteroepitaxial diffusion

Copper

Silver

Molecular dynamics

### ABSTRACT

A binary embedded-atom method (EAM) potential is optimized for Cu on Ag(111) by fitting to *ab initio* data. The fitting database consists of DFT calculations of Cu monomers and dimers on Ag(111), specifically their relative energies, adatom heights, and dimer separations. We start from the Mishin Cu–Ag EAM potential and first modify the Cu–Ag pair potential to match the FCC/HCP site energy difference then include Cu–Cu pair potential optimization for the entire database. The potential generated from this optimization method gives better agreement to DFT calculations of Cu monomers, dimers, and trimers than previous EAMs as well as a SEAM optimized potential. In trimer calculations, the optimized potential produces the DFT relative energy between FCC and HCP trimers, though a different ground state is predicted. We use the optimized potential to calculate diffusion barriers for Cu monomers, dimers, and trimers. The predicted monomer barrier is the same as DFT, while experimental barriers for monomers and dimers are lower than predicted here. We attribute the difference with experiment to the overestimation of surface adsorption energies by DFT and a simple correction is presented. Our results show that this optimization method is suitable for other heteroepitaxial systems; and that the optimized Cu–Ag EAM can be applied in the study of larger Cu islands on Ag(111).

Published by Elsevier B.V.

### 1. Introduction

Knowledge of the surface diffusion dynamics for small atom clusters is critical to understanding heteroepitaxial thin film growth. While numerous experiments [1–4] and computer simulations [5–8] have studied homogeneous systems, less is known about lattice mismatched heterogeneous systems [9–11] and their interesting diffusion kinetics. In this study, we consider Cu on Ag(111) [12], a system with a lattice mismatch of 12% [13]. The lattice mismatch induces strain in both the island and substrate and has been predicted to promote rapid diffusion [14].

To accurately compute the energetics of surface island systems, first principle density-functional theory (DFT) calculations are preferred to empirical potentials. However, DFT methods are too computationally intensive to efficiently search the phase space of each island and accurate classical potentials are needed to characterize island diffusional dynamics. The embedded-atom method [15] (EAM) is well suited for metallic systems combining pair interactions with an atomic embedding energy term dependent on the local “electron density.” Table 1 shows that other EAM potentials were unable to reproduce DFT calculated Cu island energies and geometries on Ag(111), motivating the search for a new potential.

We optimize a new EAM potential for Cu on Ag(111) using monomer and dimer DFT data. This differs from the surface

embedded-atom method (SEAM) [16,17], where the potential is optimized with respect to low index surface energies. SEAM changes the embedding energy function, while we focus on the pair potentials for the surface system. Section 2 explains the DFT and EAM calculation parameters in detail. Section 3 presents the procedure for the potential optimization and compares with previous potentials and SEAM. The energetics and diffusion results from the new EAM for monomers, dimers, and trimers are reported in Section 4. We justify the new potential for the study of small Cu islands on Ag(111) surface by comparing the calculated results to experimental and DFT values in Section 5.

### 2. Computational details

The density-functional theory calculations are performed with VASP [18,19] a density-functional code using a plane-wave basis and ultrasoft Vanderbilt-type pseudopotentials [20,21]. The local-density approximation as parameterized by Perdew and Zunger [22] and a plane-wave kinetic-energy cut-off of 200 eV ensures accurate treatment of the Cu and Ag potential. We treat the *s* and *d* states as valence, corresponding to an Ar and Kr core atomic reference configuration for Cu and Ag, respectively. The (111) surface slab calculations used a  $3 \times 3$  geometry with 6 (111) planes of Ag and 6 (111) planes of vacuum; the *k*-point meshes for the surface slab calculations are  $8 \times 8 \times 1$ , with a Methfessel–Paxton smearing of 0.25 eV.

\* Corresponding author. Tel.: +1 217 244 0670.

E-mail address: [henrywu2@illinois.edu](mailto:henrywu2@illinois.edu) (H.H. Wu).

**Table 1**  
Results for the optimized potential and other EAM potentials compared to DFT and experimental values. Three previous EAM potentials, Foiles–Baskes–Daw, Voter–Chen, and Mishin, and SEAM modified Mishin potential were compared to the optimized potential from this work with respect to monomer and dimer energies, diffusion barriers and geometries. Trimer energies for DFT and our optimized potential are also presented. The symbols indicate less than 20% error or less than 0.1 Å error (✓), between 20% and 50% error (–), and 50% error or greater than 0.1 Å error (×).  $\Delta E(A, B)$  indicates the energy difference  $E_A - E_B$ , and  $E_a(A \rightarrow B)$  indicates the activation energy to transition from state A to state B. The *ab initio* results, from ultrasoft pseudopotential DFT, are used as the standard when available. The optimized EAM potential in this work is fit to DFT values indicated by the \* symbol.

	Experiment [12]	<i>ab initio</i>	Foiles et al. [15]	Voter et al. [29–31]	Mishin et al. [27,28]	SEAM	This work					
<i>Monomer energies [meV]</i>												
$\Delta E(H, F)$	5.5 ± 1.0	14	1	×	–7	×	8	–	–267	×	12	✓*
$E_a(F \rightarrow H)$	65 ± 9	96	68	×	61	×	62	×			93	✓
<i>Dimer energies [meV]</i>												
$\Delta E(HH, FF)$		27	1	×	–11	×	15	–	811	×	27	✓*
$\Delta E(FH_{\text{short}}, FF)$		71	58	–	65	✓	79	✓	105	×	71	✓*
$\Delta E(FH_{\text{long}}, FF)$		134	66.5	×	32	×	61	×	1111	×	137	✓*
$\Delta E(FH_{\text{long}}, FH_{\text{short}})$		63	8.5	×	–33	×	–18	×	1006	×	66	✓
$E_a(FF \rightarrow HH)$	73		62	✓	42	–	69	✓			88	–
<i>Trimer energies [meV]</i>												
$\Delta E(F_{\text{non}}^3, F_{\text{rot}}^3)$		–16	41	×	49	×	33	×	63	×	9	×
$\Delta E(H_{\text{non}}^3, F_{\text{rot}}^3)$		17	38	×	30	×	50	×	29	×	42	×
$\Delta E(H_{\text{rot}}^3, F_{\text{rot}}^3)$		42	2	×	–14	×	23	×	–6	×	45	✓
$\Delta E(H_{\text{non}}^3, F_{\text{non}}^3)$		33	–3	×	–19	×	17	×	–69	×	33	✓
<i>Geometries [Å]</i>												
Dimer length		Baseline	0.036	✓	0.095	✓	0.054	✓	0.152	×	0.080	✓*
Rms error												
Adatom height		Baseline	0.115	×	0.112	×	0.153	×	0.036	✓	0.040	✓*
Rms error												

EAM energy values were computed with the LAMMPS molecular dynamics package [23]. The monomer and dimer results in Table 1 are obtained using a periodic  $3 \times 3$  cell of 6 (111) planes. The trimers are calculated with  $4 \times 4$  periodic cells. Results presented in Section 4 are from  $6 \times 6$  periodic cells, where our potential predicts a finite-size effect of less than 5 meV compared to the  $3 \times 3$  cell. Transition energy barriers are determined with nudged elastic band [24] calculations after initial and final states have been found through molecular dynamics or the dimer search method [25]. Attempt frequency prefactors are computed with the Vineyard formula [26], taking the ratio between the product of harmonic vibrational frequencies at the initial state and the saddle point.

### 3. Optimization procedure

In EAM, the total energy of the system is given by

$$E_{\text{tot}} = \frac{1}{2} \sum_{ij} \phi_{ij}(r_{ij}) + \sum_i F_i(\rho_{i,\text{tot}}), \rho_{i,\text{tot}} = \sum_{j \neq i} \rho_j(r_{ij}),$$

where  $\phi_{ij}(r_{ij})$  is the pair potential interaction between atoms  $i$  and  $j$  separated by a distance of  $r_{ij}$  and  $F_i(\rho_{i,\text{tot}})$  is embedding energy of atom  $i$  in the superposition of atomic electron densities  $\rho_j(r_{ij})$ . The Mishin CuAg binary EAM potential [27,28] is described by seven functions:  $\phi_{\text{CuCu}}(r)$ ,  $\phi_{\text{AgAg}}(r)$ ,  $\phi_{\text{CuAg}}(r)$ ,  $\rho_{\text{Cu}}(r)$ ,  $\rho_{\text{Ag}}(r)$ ,  $F_{\text{Cu}}(\rho)$ , and  $F_{\text{Ag}}(\rho)$ . The Mishin EAM embedding energy functions and electron density functions are not changed in our optimization. Only the Cu–Ag and Cu–Cu pair potentials are modified to fit our DFT optimization database. We forgo modification of the Ag–Ag potential because the distance between relaxed EAM Ag(111) planes are within 3% of the relaxed DFT Ag surface.

Cu monomers and dimers are building blocks for larger islands, making them ideal choices for the optimization database. The Ag(111) surface is divided into FCC and HCP sites, depending on the atomic configuration continuing from the top two layers of Ag. For monomers, the single Cu atom rests at either an FCC or HCP site. For dimers, four different configuration of the Cu pair

can be formed, FCC–FCC (FF), HCP–HCP (HH), and two types of FCC–HCP ( $FH_{\text{short}}$  and  $FH_{\text{long}}$ ). The two FH dimers (c.f. Fig. 5) are differentiated by their neighboring Ag atoms, the two triangles of Ag neighbors can share a side ( $FH_{\text{short}}$ ), or share a corner ( $FH_{\text{long}}$ ). The optimization database consists of the relative DFT energies between FCC and HCP monomers and all four dimers, geometric information on the heights of monomers and dimers above the Ag surface, and the Cu–Cu separation length. We minimize the total root-mean-square (rms) error of the energy differences and balance that with the total rms error of the heights and lengths.

In Fig. 1 the DFT force of a Cu atom evaporating from a perfect (unrelaxed) Ag(111) surface is plotted, and is used in addition to the database. Starting from a height of  $\frac{1}{6}[111]$ , the force on the Cu atom is computed in steps of  $\frac{1}{72}[111]$  for 13 points, then in steps of  $\frac{1}{24}[111]$  until  $[111]$ , where the DFT force dropped to zero. The Cu atom is directly above FCC and HCP sites to cancel forces in the (111) plane. The difference in force between FCC and HCP is less than 0.04 eV/Å for both DFT (max deviation at  $\frac{1}{2}[111]$ ) and EAM (max deviation at  $\frac{2}{3}[111]$ ). Fig. 1 shows that DFT has a stronger binding of Cu to the Ag surface than the Mishin EAM. Also plotted in Fig. 1 is the force calculated with our optimized EAM, which captures the deeper and wider well of DFT forces.

Fig. 2 shows the Cu–Ag pair potential extracted from force-matching to the DFT data. Starting from the highest point and moving towards the surface, the Cu atom feels the sum of forces from different shells of Ag atoms within a 7.2 Å cut-off radius. We chose this cut-off radius because the DFT forces goes to zero at  $z = 7 \text{ Å}$  ( $[111]$ ). For each  $z_k$ , there are  $m = 1, \dots, m_k$  shells, in which there are  $n_m$  Ag atoms at distance  $r_{k,m}$  with directional component  $c_{k,m} = \frac{\partial r_{k,m}}{\partial z} \Big|_{z_k}$ . The z-component of the force at height  $z_k$  is

$$F_z(z_k) = -\frac{\partial E_{\text{tot}}}{\partial z} = \sum_{\text{all atoms}} \frac{-\partial E_{\text{tot}}}{\partial r} \frac{\partial r}{\partial z} = \sum_{m=1}^{m_k} -n_m c_{k,m} \phi'_{\text{CuAg}}(r_{k,m}), \quad (1)$$

where  $\phi'_{\text{CuAg}}(r_{k,m})$  is the radial derivative of the pair potential. We build the function  $\phi'_{\text{CuAg}}(r)$  as a cubic spline with knot points

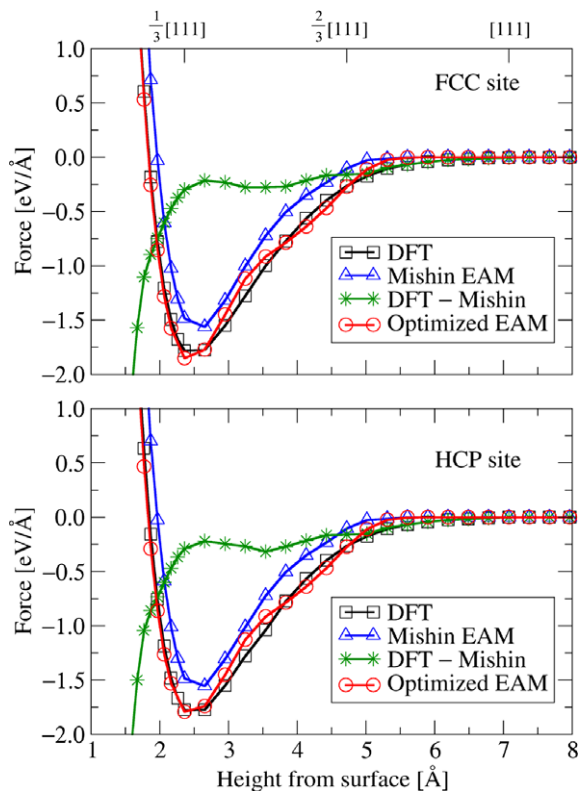


**Fig. 1.** Force on a Cu atom above an FCC site or an HCP site on the unrelaxed Ag(111) surface calculated by DFT, Mishin EAM, and the new optimized EAM. The ultrasoft pseudopotential DFT force displays a stronger and wider interaction between the Cu atom and the Ag surface than Mishin EAM. The average force difference (FCC and HCP) between DFT and Mishin EAM is used to produce the force-matched  $\phi_{\text{CuAg}}(r)$  in Fig. 2. The final optimized EAM potential deviates between 3 Å and 5 Å with a maximum deviation of 0.15 eV/Å with respect to the DFT calculated forces.

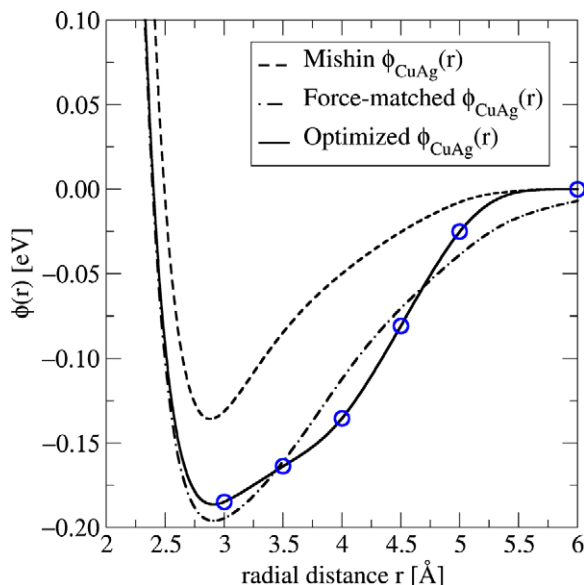


**Fig. 2.** The Cu–Ag pair potential at sequential steps in the optimization process. The integrated force difference from Fig. 1 adds onto the original Mishin  $\phi_{\text{CuAg}}(r)$  to produce the force-matched  $\phi_{\text{CuAg}}(r)$ . Imposing a smooth cut-off at 6 Å and adding a spline (knots at circles) to the force-matched potential produces the optimized  $\phi_{\text{CuAg}}(r)$ . The spline knots are at 3 Å, 3.5 Å, 4 Å, 4.5 Å, 5 Å, and 6 Å.

$r_k^{\text{knot}} = \min\{r_{k,m}\}$  for each  $k$ . Starting from largest  $z_k$  to smallest, Eq. (1) is solved for  $\phi'_{\text{CuAg}}(r_k^{\text{knot}})$  using, as needed, interpolated values of

$\phi'_{\text{CuAg}}(r)$  for  $r > r_k^{\text{knot}}$ . The equations are solved successively until  $\phi_{\text{CuAg}}$  is self-consistent. A final self-consistency loop over all FCC and HCP forces is performed, alternating in sequence, obtaining  $\phi'_{\text{CuAg}}(r)$  for  $r$  in the range from 2.04 Å to 7.2 Å. Integrating  $\phi'_{\text{CuAg}}(r)$  generates a quartic spline, the  $\phi_{\text{CuAg}}(r)$  plotted in Fig. 2. This force-matched  $\phi_{\text{CuAg}}(r)$  possess a deeper and wider energy well, capturing the stronger Cu–Ag interaction from DFT. For  $r$  values smaller than 2.04 Å, we linearly extrapolate  $\phi_{\text{CuAg}}(r)$ .

The force-matched  $\phi_{\text{CuAg}}(r)$  is refined by fitting to the monomer and dimer database. The force-matched  $\phi_{\text{CuAg}}(r)$  has inaccurate energies for monomers and dimers, with the HCP site 4 meV below the FCC site. Modifying  $\phi_{\text{CuCu}}(r)$  does not affect monomer energies, and we find that the dimer energy difference between FF and HH changes by less than 5 meV with the  $\phi_{\text{CuCu}}(r)$  modifications we present later. We optimize the Cu–Ag pair potential with respect to monomer and homogeneous dimer site energy differences as the next step. We reduce the interaction range to 6 Å by shifting the potential up by  $\phi$  (5.75 Å) and using quartic splines from 5 Å to 6 Å. The quartic splines have two equal spaced knots within the interval and matches the value, first and second derivatives at 5 Å, and at 6 Å goes to zero with zero slope and zero second derivative. To differentiate between FCC and HCP sites, we modify the Cu–Ag interaction in the range of the second and third nearest neighbors for a Cu atom on the surface by adding a cubic spline, with knots at 3.5 Å, 4 Å, 4.5 Å, 5 Å, and fixed end points at 3 Å and 6 Å. We generate  $(2 \times 5 + 1)^4 = 14,641$  possible potentials with different values at each knot point in steps of  $\pm 20$  meV; optimization continues using narrower ranges down to  $\pm 1$  meV. For each sweep, we select potentials with the smallest rms monomer and homogeneous dimer energy errors while also selecting for quantitatively low rms Cu height errors and potentials without multiple minimums. In Fig. 2, this optimized  $\phi_{\text{CuAg}}(r)$  exhibits a wider well than the force-matched pair potential.

Fig. 3 shows that the optimized  $\phi_{\text{CuCu}}(r)$  gives shorter and weaker bonding between Cu atoms on the Ag surface than in the Mishin EAM bulk Cu. We scale the original Mishin  $\phi_{\text{CuCu}}(r)$  in 1% steps from 80% to 120%, and translate in 0.01 Å steps from  $-0.15$  Å to 0.15 Å; potentials with Cu lattice parameter outside of  $\pm 5\%$  of the bulk value are removed. A 82% scaling and a  $-0.13$  Å translation reproduces all relative energy differences with a final 0.5 meV range optimization of the  $\phi_{\text{CuAg}}(r)$ . We found during optimization that although it was possible to obtain 0.012 Å rms dimer separation error or 0.5 meV rms energy error, these two errors grew opposite one another. We selected for lower energy error at the expense of geometric agreement.

Thus, our optimization procedure with respect to DFT Cu monomers and dimers follows: (1) Modify the  $\phi_{\text{CuAg}}(r)$  to match the force of an evaporating Cu atom from Ag(111) calculated in DFT. (2) Reduce the interaction length of the force-matched  $\phi_{\text{CuAg}}(r)$  and add splines to reproduce the DFT FCC/HCP site energy difference. (3) Scale and translate the  $\phi_{\text{CuCu}}(r)$  to produce better energetic agreement. (4) Polish the optimized  $\phi_{\text{CuAg}}(r)$  potential with the optimized  $\phi_{\text{CuCu}}(r)$ . The final  $\phi_{\text{CuAg}}(r)$  is plotted in Fig. 2, and  $\phi_{\text{CuCu}}(r)$  in Fig. 3. The Cu–Ag (111) EAM potential optimized in this work can be obtained from the NIST Interatomic Potentials Repository [32].

In Table 1, comparison with other EAM potentials show that the optimized EAM from this work has better agreement to DFT calculations. Among the earlier potentials, the Mishin EAM [27,28] comes closest to the DFT energies when compared to the Foiles–Baskes–Daw (FBD) EAM [15] and the Voter–Chen (VC) EAM [29,30] with Sprague [31] alloy potential. The FBD potential did not indicate any site energy difference between FCC and HCP, while the VC potential shows the HCP sites as more stable. None of the earlier potentials were able to capture the correct DFT energy difference between  $\text{FH}_{\text{short}}$  and  $\text{FH}_{\text{long}}$  dimers. All three

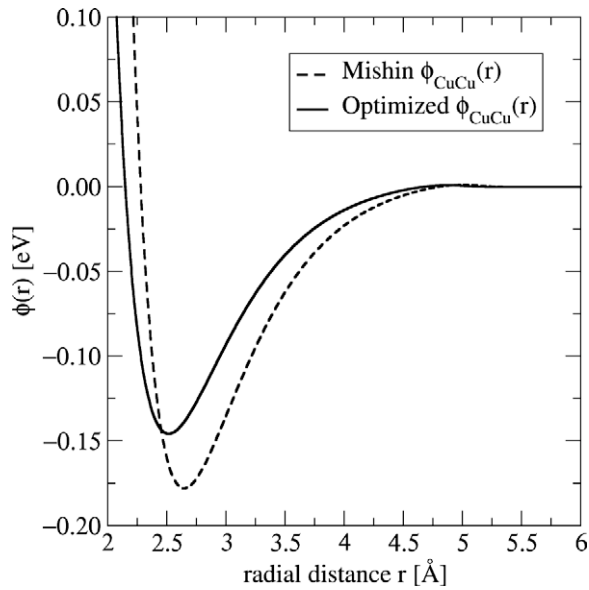


**Fig. 3.** The Cu–Cu pair potential from Mishin EAM and after optimization. The original Mishin  $\phi_{\text{CuCu}}(r)$  is transformed with different scalings and translations simultaneously with the optimization of the  $\phi_{\text{CuAg}}(r)$ . The optimized  $\phi_{\text{CuCu}}(r)$  is obtained from a scaling of 82% and a translation of  $-0.13 \text{ \AA}$ . This indicates shorter and weaker bonding between Cu atoms on the Ag surface than in Cu bulk.

potentials produce monomer barriers close to that of experiment; in addition, the FBD and Mishin potentials also comes close to the experimental dimer diffusion barrier. The optimized EAM potential overestimates the experimental barriers but correctly predicts the DFT monomer diffusion barrier. We constructed the SEAM potential from the Mishin EAM based on procedures by Haftel [16]. The results from the SEAM shows very poor agreement with the DFT values. The increased Cu–Ag interaction of the optimized potential were able to pull the Cu atoms closer to the Ag surface, reducing the rms height error over other potentials. While the earlier potentials do not come close to the DFT trimer energies, the optimized EAM is able to capture the correct energies for  $\Delta E(H_{\text{rot}}^3, F_{\text{rot}}^3)$  and  $\Delta E(H_{\text{non}}^3, F_{\text{non}}^3)$ . The deviation for the trimer ground state will be discussed in Section 5.

An alternative approach to producing optimized potentials for surface applications—SEAM—is unable to provide an accurate Cu–Ag(111) potential. SEAM modifies the embedding energy function with additional energy penalties applied to electron densities deviating from the bulk value. Following the SEAM methodology [16], we modified the Mishin EAM to match DFT (111) and (100) surface energies for both Cu and Ag (Table 2). The results in Table 1 show the HCP monomer site as more stable than the FCC site; this is due to the close Ag atom directly under the HCP site being penalized less than those in an FCC site. The electron densities experienced

by surface islands are outside those optimized in SEAM, the same way that electron densities experience by surfaces are outside those optimized in bulk EAM. Because of SEAM error propagation and amplification in island geometries, we conclude that for Cu–Ag(111), a direct optimization of pair potentials to island energies performs better.

#### 4. Results

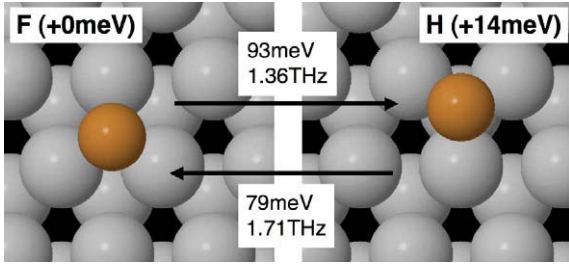
Fig. 4 shows the geometries, relative energies, and transition barriers of Cu monomers calculated with the optimized EAM. The 14 meV energy difference between the FCC and HCP site also represents the difference between the transition barriers. The two transitions possible are the  $F \rightarrow H$  with a 93 meV barrier and the 79 meV barrier  $H \rightarrow F$  transition. The  $F \rightarrow H$  barrier is higher than the experimental value of  $65 \pm 9 \text{ meV}$  [12], but matches our DFT calculations for the bridging site with an energy difference of 96 meV. DFT is known to overestimate surface adsorption [35], and we discuss strategies to compensate in Section 5. The agreement with DFT is a confirmation of our potential since the bridging site energy is not part of the optimization database.

Fig. 5 shows the geometries, relative energies, and transition barriers of Cu dimers calculated with the optimized EAM. The FF dimer is the ground state and the HH dimer is 26 meV higher in energy, about twice the monomer energy difference. The  $FH_{\text{short}}$  and  $FH_{\text{long}}$  dimers are two metastable configurations which are 78 meV and 130 meV higher in energy than FF, respectively. Dimer diffusion is more complex than that for monomers, with two intermediate states between FF and HH plus dimer rotation. With low barrier ( $<1 \text{ meV}$ ) transitions out of the  $FH_{\text{long}}$  state, the diffusion pathway through  $FH_{\text{long}}$  has a 130 meV barrier for  $FF \rightarrow FH_{\text{long}} \rightarrow HH$ , and 103 meV barrier for  $HH \rightarrow FH_{\text{long}} \rightarrow FF$ . The other diffusion pathway is more complicated, since an  $FH_{\text{short}}$  dimer is more likely to transition to FF (2 meV barrier) than to HH (10 meV barrier). This results in a 88 meV barrier for  $FF \rightarrow FH_{\text{short}} \rightarrow HH$  ( $88 \text{ meV} - 2 \text{ meV} + 10 \text{ meV}$ ), and 62 meV barrier for  $HH \rightarrow FH_{\text{short}} \rightarrow FF$ . The calculated barriers are higher than the experimental barrier of 73 meV [12], again consistent with overestimated adsorption energies by DFT.

Fig. 6 shows the geometries, relative energies, and transition barriers of Cu trimers calculated with the optimized EAM. There are two different configurations for each of the FCC and HCP trimers due to the geometry of the (111) surface. The trimer triangles can either be centered around a surface Ag atom permitting rotation,  $F_{\text{rot}}^3$  (ground state) and  $H_{\text{rot}}^3$  (+45 meV), or not,  $F_{\text{non}}^3$  (+9 meV) and  $H_{\text{non}}^3$  (+42 meV). The relative energy difference between  $F^3$  and  $H^3$  trimers is approximately two to three times the monomer energy difference. The rotation transition  $F_{\text{rot}}^3 \rightarrow H_{\text{rot}}^3$  has a 149 meV barrier and a 104 meV barrier for the reverse. The non-rotatable trimers do not rotate, and transition to rotatable trimers on the opposite sites. These transition barriers are higher than the rotation barriers, at  $\sim 290 \text{ meV}$  from  $F_{\text{non}}^3 \rightarrow H_{\text{rot}}^3$  and  $F_{\text{rot}}^3 \rightarrow H_{\text{non}}^3$ , and

**Table 2**  
SEAM parameters ( $\Delta$  and  $C$ ) and surface energies of Ag and Cu. The original Ag and Cu embedding functions come from the Mishin EAM potential [27,28]. The choice of  $\Delta$  and  $C$  reproduce surface energies ((111) and (100)) as closely as possible. The embedding energy function is modified whenever the normalized electron density ( $\rho$ ) is more than  $\Delta$  away from the normalized equilibrium bulk value ( $\rho_{\text{bulk}} = 1.0$ ). The amount added to the embedding function is given by  $C(|\rho - 1| - \Delta)^2$  as in [16].

	$\Delta$	$C$ [eV]		Surface energy [mJ/m <sup>2</sup> ]		
				DFT [33,34]	Mishin et al. [27,28]	SEAM
Ag	0.025	6.0	(111)	1210	862	1062
			(100)	1210	940	1254
Cu	0.05	1.5	(111)	1294	1239	1290
			(100)	1478	1345	1454



**Fig. 4.** Cu monomers FCC (F) and HCP (H), relative energy differences, transition energies, and attempt frequency prefactors. The FCC site is the ground state and can diffuse to one of three equivalent HCP sites nearby; similarly the HCP site diffuses to one of three FCC sites. The rate-limiting step in the diffusion process is the  $F \rightarrow H$  transition with an energy barrier of 93 meV.

$\sim 250$  meV for the reverse. We expect, as with monomers and dimers, that the EAM overestimates the trimer transition barriers.

We construct analytical expressions for the diffusion constants of monomers, dimers, and trimers using the calculated transition barriers and attempt frequencies. The rate of jumping from an F site to a particular H site is  $r_{FH} = \nu_{F \rightarrow H} \exp(-E_a(F \rightarrow H)/k_B T)$  where  $E_a(F \rightarrow H)$  and  $\nu_{F \rightarrow H}$  are the energy barrier and the attempt frequency for the F to H transition. Then a monomer moving from one F to a new F site through an H site at temperature  $T$  occurs with mean wait time of

$$\tau_{\text{monomer}} = \frac{3}{2} [(3r_{FH})^{-1} + (3r_{HF})^{-1}],$$

including the three equivalent hopping sites for each monomer transition, and with a correlation factor of  $\frac{3}{2}$  for monomer transitions to the original site. The Einstein diffusion relation,  $D = \frac{1}{4} a_{nn}^2 \tau^{-1}$ , where  $a_{nn} = 2.89 \text{ \AA}$  is the nearest-neighbor distance between Ag atoms gives the monomer diffusion constant

$$D_{\text{monomer}} = \frac{a_{nn}^2}{2} [(r_{FH})^{-1} + (r_{HF})^{-1}]^{-1}.$$

For both the dimer and trimer case, the diffusion system becomes complex and we use the continuous-time random walk formalism developed by Shlesinger and Landman [36]. The diffusion constant for the dimer is computed numerically and plotted in Fig. 7, while the diffusion constant for the trimer is given by

$$D_{\text{trimer}} = \frac{a_{nn}^2}{2} \frac{r_{F_{\text{non}}^3 H_{\text{rot}}^3} r_{H_{\text{non}}^3 F_{\text{rot}}^3} (r_{F_{\text{rot}}^3 H_{\text{rot}}^3 r_{H_{\text{rot}}^3 F_{\text{non}}^3} + r_{F_{\text{rot}}^3 H_{\text{non}}^3} r_{H_{\text{rot}}^3 F_{\text{rot}}^3})}{r_{F_{\text{rot}}^3 H_{\text{rot}}^3} r_{H_{\text{non}}^3 F_{\text{rot}}^3} r_{H_{\text{rot}}^3 F_{\text{non}}^3} + r_{F_{\text{non}}^3 H_{\text{rot}}^3} (r_{F_{\text{rot}}^3 H_{\text{rot}}^3} r_{H_{\text{non}}^3 F_{\text{rot}}^3} + (r_{F_{\text{rot}}^3 H_{\text{non}}^3} + r_{H_{\text{non}}^3 F_{\text{rot}}^3}) r_{H_{\text{rot}}^3 F_{\text{rot}}^3})}.$$

In Fig. 7, the analytical rates from above have been plotted as diffusion coefficients against temperature along with experimental data from [12] for the monomer and dimer. The experimental barriers,  $65 \pm 9$  meV and 73 meV for monomer and dimer are both lower than our calculated values, though no error bar is given for the dimer experimental barrier. The rate-limiting barriers as  $T \rightarrow 0$  K are calculated using data at  $T < 20$  K. The rate-limiting barriers, 93 meV, 88 meV, and 289 meV, correspond to the rate-limiting transition barriers identified above for the monomer, dimer, and trimer. The dimer diffusion slope decreases with increasing temperature due to the influence of both FH intermediate states. Higher temperatures samples the  $FH_{\text{long}}$  pathway; this decreases dimer diffusion as transitions through the  $FH_{\text{long}}$  state lead to rotation, i.e.,  $FF \rightarrow FH_{\text{long}} \rightarrow HH \rightarrow FH_{\text{long}} \rightarrow FF$ . The prefactors for transitions out of  $FH_{\text{short}}$  are the lowest for all dimer transitions, and become rate limiting at high temperatures.

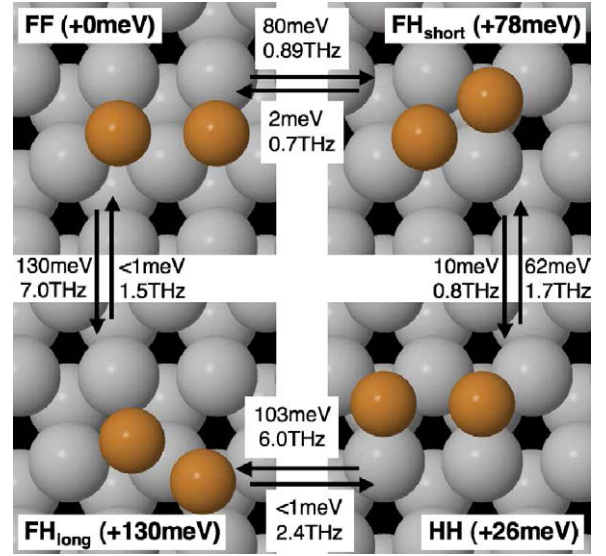


**Fig. 5.** Cu dimers FCC-FCC (FF), FCC-HCP neighboring ( $FH_{\text{short}}$ ), FCC-HCP non-neighboring ( $FH_{\text{long}}$ ), and HCP-HCP (HH), relative energy differences, transition energies, and attempt frequency prefactors. The FF dimer is the ground state and diffusion to the HH site is achieved through one of two FH meta-stable sites. The pathway through the  $FH_{\text{short}}$  dominates the  $FF \leftrightarrow HH$  diffusion, giving an overall rate-limiting barrier of 88 meV ( $FF \rightarrow FH_{\text{short}} \rightarrow HH$ , 80 meV – 2 meV + 10 meV).

## 5. Discussion

The Cu monomer is the basic unit for Cu islands on Ag(111), and the correct extrapolation of monomer energies and barriers to dimers and trimers indicates the optimized potential is consistent with DFT. For the monomer, the site energy difference between FCC and HCP is 14 meV, twice the difference is seen between the homogeneous dimers FF and HH at 26 meV, and two to three times the difference in the rotatable and non-rotatable trimer pairs at 33 meV and 45 meV. The diffusion barriers for the trimer are also three times that of the monomer, 289 meV versus 93 meV and 247 meV versus 79 meV. This linear relationship is explained by the fact that in the trimer diffusional transitions, all

three atoms move simultaneously over each of their respective bridging sites, thus the trimer as a whole experiences a barrier three times as large. In the dimer system, diffusion moves one atom at a time and the barrier is comparable to that of the monomer.

EAM produces higher diffusion barriers for monomer and dimer than in experiment [12], but gives diffusion barriers that match DFT. This effect is consistent with the observed overestimation of surface adsorption energy by DFT calculations [35]. Compared to experiments for monomer and dimer, the barriers are overestimated by approximately 10–15 meV. Since diffusion for both the monomer and dimer proceeds one Cu atom at a time, we expect the bridging site between F and H to be overestimated by 15 meV. For general diffusion barriers, a 15 meV reduction should be applied for each concurrent Cu atom in the transition when comparing to experiment. For example, a threefold reduction of 45 meV will need to be applied to the trimer diffusion barriers.

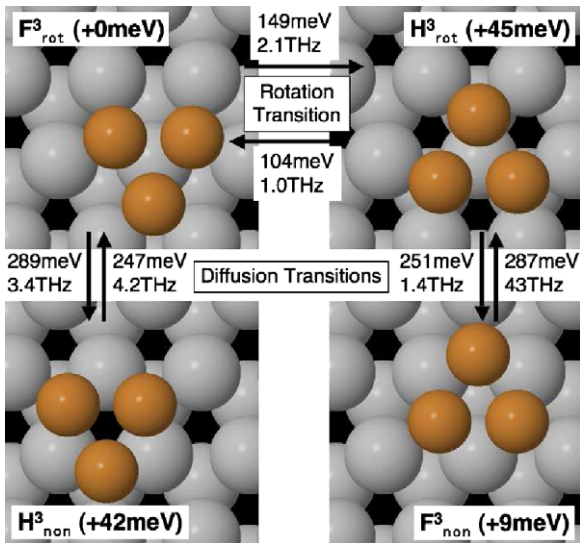


**Fig. 6.** Cu trimers FFF centered on Ag ( $F_{rot}^3$ ), HHH centered on Ag ( $H_{rot}^3$ ), HHH centered on a hole ( $H_{non}^3$ ), and FFF centered on a hole ( $F_{non}^3$ ), relative energy differences, transition energies, and attempt frequency prefactors.  $F_{rot}^3$  is the ground state but is only 9 meV lower in energy than the  $F_{non}^3$  state. A rotation transition exists between  $F_{rot}^3$  and  $H_{rot}^3$ , while the system can diffuse by overcoming the higher 289 meV and 287 meV energy barriers for  $F_{rot}^3 \rightarrow H_{non}^3$  and  $H_{rot}^3 \rightarrow F_{non}^3$  respectively.

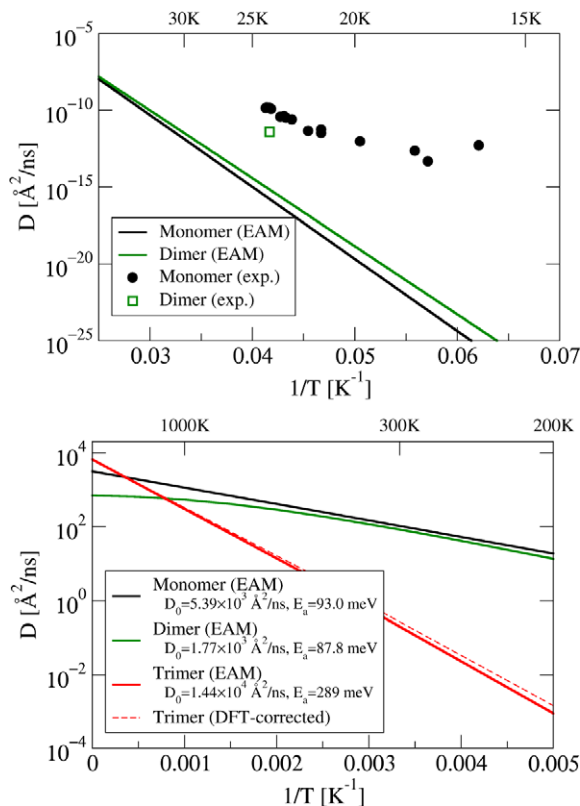


**Fig. 7.** Experimental results for monomer and dimer compared with analytical diffusion calculations for monomer, dimer, trimer, and DFT corrected trimer at low (top) and high (bottom) temperatures. The Arrhenius fit, in the  $T \rightarrow 0$  K limit, for the monomer, dimer, and trimer systems reflects the rate-limiting diffusion barriers 93 meV, 88 meV, and 289 meV respectively. The DFT corrected trimer is calculated by adjusting the trimer diffusion barriers to match DFT energy differences and keeping the same prefactors. The experimental monomer barrier is  $65 \pm 9$  meV from data in the temperature range 19–25 K. The experimental dimer barrier is 73 meV from data at 24 K assuming a prefactor of 1 THz.

Despite not being in our optimization database, trimer energies can be predicted reasonably well with out new potential. The main discrepancy with DFT is with the trimer ground state. DFT calculates that the two non-rotatable trimers are 25 meV lower in energy than predicted by our optimized EAM, making the ground state trimer configuration  $F_{non}^3$  rather than  $F_{rot}^3$ . We expect the deviation to be mainly caused by the center Ag atom under the rotatable trimer, whose embedded electron density is 16% higher than an Ag atom in the bulk. This density is beyond the range present in the monomer and dimer database. Modifying the embedding function like in SEAM can penalize this relatively high density, but the optimization would need to be fit for a wider range of electron density values.

Although the relative energy between rotatable and non-rotatable trimers are not correct, the optimized EAM correctly predicts the energy difference between  $F_{rot}^3$  and  $H_{rot}^3$ , and  $F_{non}^3$  and  $H_{non}^3$ . Adding a Cu atom to a rotatable trimer will create a non-rotatable trimer subsection, and in larger islands, this pairing of rotatable and non-rotatable trimers allows the correct energy differences to be calculated. We expect the trimer diffusion barrier to remain three times that of the monomer even with the change in ground state. A new estimate of trimer diffusion can be computed by splitting the 25 meV energy difference between forward and reverse diffusion barriers, e.g. lower the rotatable to non-rotatable barrier by 12.5 meV and raising the non-rotatable to rotatable by 12.5 meV. This change does not affect the transition paths and therefore does not change the overall diffusional dynamics of the trimer system, increasing the rate-limiting barrier to 292 meV from 289 meV (c.f. Fig. 7). Applying the 45 meV over-adsorption correction gives a barrier of 247 meV for trimer diffusion to compare with experiment.

## 6. Conclusion

We present a method to optimize an EAM potential for heterogeneous surface system using *ab initio* data. The potential from this optimization method produce a better match to DFT energies of Cu monomers, dimers, and trimers on Ag(111) than previous EAMs and SEAM. Diffusion barriers for monomers, dimers, and trimers are calculated to be 93 meV, 88 meV, and 289 meV, which match available DFT data, but exceed experimental values. To correct for the overestimated barriers, a 15 meV reduction is applied for each concurrently transitioning Cu atom. We found a 25 meV energy discrepancy between rotatable and non-rotatable trimers when compared with DFT. This discrepancy is not worse for larger islands due to correct energy difference between F-trimers and H-trimers calculated by the potential compared with DFT. We expect the new EAM potential to accurately describe the diffusion and energetics of larger Cu islands on Ag(111). Moreover, the general potential optimization approach should be applicable for other heteroepitaxial systems.

## Acknowledgments

The authors thank John Weaver and Andrew Signor for helpful discussions. This research was supported by NSF/DMR Grant 0703995, and 3M's Untenured Faculty Research Award.

## References

- [1] J.-M. Wen, S.-L. Chang, J.W. Burnett, J.W. Evans, P.A. Thiel, Phys. Rev. Lett. 73 (19) (1994) 2591.
- [2] G.L. Kellogg, A.F. Voter, Phys. Rev. Lett. 67 (1991) 622–625.
- [3] M.C. Bartelt, C.R. Stoldt, C.J. Jenks, P.A. Thiel, J.W. Evans, Phys. Rev. B 59 (1999) 3125–3134.
- [4] G. Antczak, G. Ehrlich, Surf. Sci. Rep. 62 (2007) 39–61.
- [5] N.I. Papanicolaou, G.A. Evangelakis, G.C. Kallinteris, Comput. Mater. Sci. 10 (1998) 105–110.
- [6] F. Montalenti, R. Ferrando, Phys. Rev. B 59 (1999) 5881–5891.

- [7] A. Bogicevic, Phys. Rev. Lett. 82 (26) (1999) 5301.
- [8] H.T. Lorensen, J.K. Nørskov, K.W. Jacobsen, Phys. Rev. B 60 (8) (1999) R5149.
- [9] V. Chirita, E. Munger, J. Greene, J.-E. Sundgren, Surf. Sci. Lett. 436 (1999) L641–L647.
- [10] V. Papatlanakos, G.A. Evangelakis, Surf. Sci. 499 (2002) 229–243.
- [11] H. Brune, G.S. Bales, J. Jacobsen, C. Boragno, K. Kern, Phys. Rev. B 60 (8) (1999) 5991.
- [12] K. Morgenstern, K.-F. Braun, K.-H. Rieder, Phys. Rev. Lett. 93 (5) (2004) 056102.
- [13] V. Ozoliņš, C. Wolverton, A. Zunger, Phys. Rev. B 57 (1998) 4816–4828.
- [14] J.C. Hamilton, Phys. Rev. Lett. 77 (1996) 885–889.
- [15] S.M. Foiles, M.I. Baskes, M.S. Daw, Phys. Rev. B 33 (12) (1986) 7983–7991.
- [16] M.I. Haftel, Phys. Rev. B 48 (4) (1993) 2611.
- [17] M.I. Haftel, M. Rosen, Phys. Rev. B 51 (1995) 4426.
- [18] G. Kresse, J. Hafner, Phys. Rev. B 47 (1) (1993) RC558–561.
- [19] G. Kresse, J. Furthmüller, Phys. Rev. B 54 (16) (1996) 11169–11186.
- [20] D. Vanderbilt, Phys. Rev. B 41 (11) (1990) 7892–7895.
- [21] G. Kresse, J. Hafner, J. Phys. Condens. Mater. 6 (40) (1994) 8245–8257.
- [22] J.P. Perdew, A. Zunger, Phys. Rev. B 23 (1981) 5048–5079.
- [23] S.J. Plimpton, J. Comp. Phys. 117 (1995) 1–19. <<http://lammps.sandia.gov/>>.
- [24] G. Mills, H. Jónsson, Phys. Rev. Lett. 72 (7) (1994) 1124–1127, doi:10.1103/PhysRevLett.72.1124.
- [25] G. Henkelman, H. Jónsson, J. Chem. Phys. 111 (1999) 7010–7022.
- [26] G.H. Vineyard, J. Phys. Chem. Solids 3 (1957) 121–127.
- [27] Y. Mishin, M.J. Mehl, D.A. Papaconstantopoulos, A.F. Voter, J.D. Kress, Phys. Rev. B 63 (22) (2001) 224106, doi:10.1103/PhysRevB.63.224106.
- [28] P.L. Williams, Y. Mishin, J.C. Hamilton, Modell. Simul. Mater. Sci. Eng. 14 (5) (2006) 817–833.
- [29] A.F. Voter, S.P. Chen, Mater. Res. Soc. Symp. Proc. 82 (1987) 175.
- [30] A.F. Voter, Embedded atom method potentials for seven FCC metals: Ni, Pd, Pt, Cu, Ag, Au, Al, Los Alamos Unclassified Technical Report, 1993.
- [31] J.A. Sprague, F. Montalenti, B.P. Uberuaga, J.D. Kress, A.F. Voter, Phys. Rev. B 66 (2002) 205415.
- [32] C. Becker, NIST Interatomic Potentials Repository. <<http://www.ctcms.nist.gov/potentials>>.
- [33] M. Methfessel, D. Hennig, M. Scheffler, Phys. Rev. B 46 (1992) 4816–4829.
- [34] J. Yu, S.B. Sinnott, S.R. Phillpot, Philos. Mag. Lett. 89 (2) (2009) 136–144.
- [35] C. Stampfl, Catal. Today 105 (2005) 17–35.
- [36] M.F. Shlesinger, U. Landman, Applied Stochastic Processes, Academic Press, New York, 1980.